Electrostatic Fringing-Field Actuation for Pull-In Free RF-MEMS Analog Tunable Resonators

J Small[1], W Irshad[1], A Fruehling[1], X Liu[2], A Garg[1] and D Peroulis[1]

[1] Birck Nanotechnology Center and the School of Electrical and Computer Engineering, Purdue University, West Lafayette, IN 47906 United States of America
[2] School of Electrical and Computer Engineering, University of California, Davis, CA 95616 United States of America

E-mail: `smallj@purdue.edu`

Abstract. This paper presents the design, fabrication, and measurement of the first pull-in free tunable evanescent-mode microwave resonator based on arrays of electrostatically actuated fringing-field RF-MEMS tuners. Electrostatic fringing-field actuation (EFFA) is key on achieving a wide tunable frequency range that is not limited by the conventional pull-in instability. Furthermore, total lack of dielectric layers and no overlap between the pull-down electrode and movable beams significantly enhances the robustness of our proposed tuning mechanism by making it devoid of dielectric charging and stiction and amenable to high-yield manufacturing. The proposed electrostatic fringing-field tuners are demonstrated in a highly-loaded evanescent-mode cavity-based resonator. The measured unloaded quality factor is $280-515$ from $12.5-15.5$ GHz. In addition, a $10\times$ improvement in switching time is demonstrated for the first time for EFFA tuners in a tunable microwave component by employing DC-dynamic biasing waveforms. With dynamic biasing, the measured up-to-down and down-to-up switching time of the resonator are 190 μs and 148 μs, respectively. On the other hand, conventional step biasing results in switching times of 5.2 ms and 8 ms for up-to-down and down-to-up states, respectively.
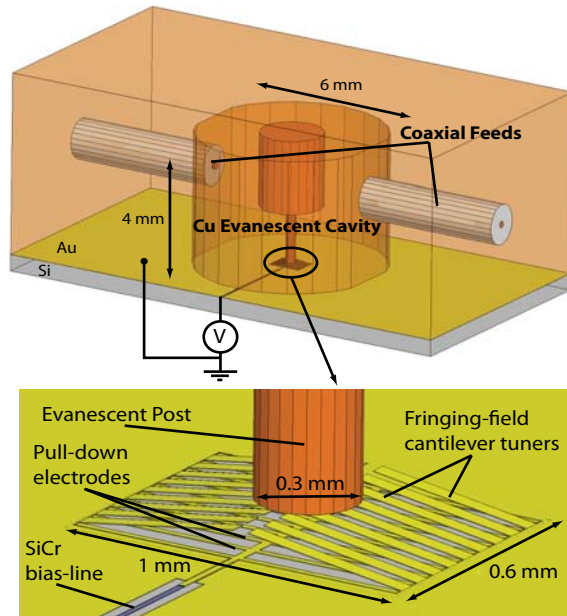
Figure 1. 3D schematic of the tunable resonator based on EFFA RF-MEMS tuners.

1. Introduction

Evanescent mode tunable resonators have been demonstrated with piezoelectric [1] and electrostatic microelectromechanical systems (MEMS) tuners [2] - [11]. Piezoelectrically tuned resonators yield excellent radio frequency (RF) results. However, the tuners typically have slow tuning speed ($\sim$ 1 ms) and are relatively large. Electrostatically tuned resonators can be made smaller [3], and made of materials that exhibit nearly zero hysteresis and drift [4]. In particular, electrostatic RF-MEMS have demonstrated excellent unloaded quality factor, Q_u, (50−1850) and capacitance tuning ratios, C_r, (2−100) [2] - [11]. Electrostatic RF-MEMS also exhibit switching times of 10s of μs, very high linearity ($>$ 60 dBm), good power handling (1−10 W), and virtually zero power consumption [12]. Temperature insensitive designs have also been recently experimentally demonstrated [13] and [14]. Lastly, experimental validation of the vibration tolerance of RF-MEMS tunable resonators has shown encouraging results [10]. However, the tuning range of electrostatic analog tunable RF-MEMS resonators is limited by the well known pull-in instability.

Electrostatic fringing-field actuated MEMS tuners are an attractive alternative because they do not suffer from pull-in instability [15]. The stable and continuous gap height versus voltage characteristics is ideal for analog frequency selection in RF front ends. Replacing a solid diaphragm by an array of cantilever beams has been shown to not severely degrade the Q_u [10] and [11]. Furthermore, when compared to MEMS tuning diaphragms, our presented technique is less susceptible to shock, acceleration, and vibration due to the three-orders-of-magnitude reduced mass [10]. However, attention needs to be paid to the resulting tradeoffs between Q_u and switching time.
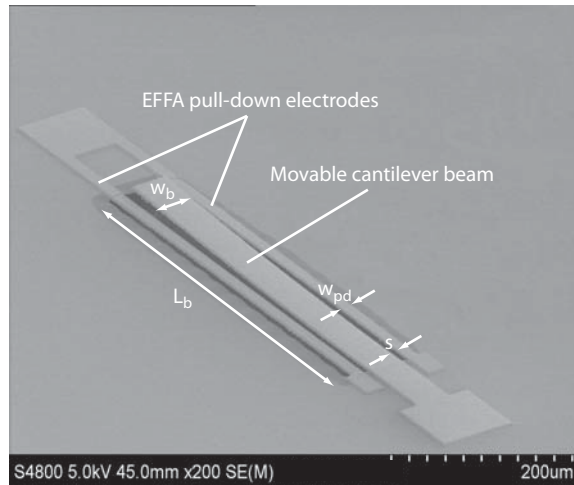
Figure 2. Scanning electron micrograph of electrostatic fringing-field actuated tuner for pull-in free frequency tuning.

This paper investigates these issues for the first time. We present a pull-in free RF-MEMS analog tunable resonator that merges the high-Q_u and frequency reconfigurability capabilities of the evanescent-mode cavity-based resonator with the robust device design of electrostatic fringing-field MEMS actuators. Detailed device design information for fringing-field tuned resonators is first presented. Next, the fabrication, resonator assembly, and RF measurement is presented. The measured Q_u of a static cavity with cantilevers is 34 % smaller compared to the simulated cavity with a solid diaphragm. A tunable resonator is demonstrated with EFFA MEMS and exhibits a Q_u of $280-515$ from $12.5-15.5$ GHz (tuning range of 21.4 %). Finally, the switching time with $10\times$ improvement with the use of DC-dynamic biasing waveforms is reported for the first time for EFFA tunable resonators.

2. Design

2.1. Proposed Resonator

Figure 1 illustrates a 3D schematic of the proposed EFFA MEMS tuned cavity-based resonator. An evanescent-mode cavity resonator is used as a vehicle to demonstrate the proposed concept due to the highly concentrated electric field residing between the ceiling of the cavity and the top of the post. When this gap is on the order of micrometers, a deflection of a few micrometers corresponds to a frequency shift on the order of gigahertz [4]. In the proposed design the cantilever beams bend naturally upwards after they are released due to their non-zero stress (figure 2). In particular, their linear post-release profile is attributed to the composite Au/SiO$_2$ anchor as predicted by simulations based on [16]. Fringing-field actuation is accomplished by having each cantilever beam fenced by a stiff fixed-fixed beam on each side as illustrated in figures 1 and 2.

Table 1. Parameters for Electrostatic Fringing-Field Tunable Evanescent-Mode Resonator

Parameter	Symbol	Value
Capacitive post diameter (μm)	$\varnothing_{post}$	300
Cantilever beam length (μm)	L_b	500
Cantilever beam width (μm)	w_b	50
Cantilever beam thickness (μm)	t_b	2
Pull-down electrode width (μm)	w_{pd}	20
Horizontal gap (μm)	s	5
Initial actuation tip height (μm)	h_0	50
Initial capacitive gap (μm)	g_{rf}	5

2.2. RF Design

A Ku-band tunable resonator with $Q_u > 800$ and frequency tuning of > 50 % is designed to demonstrate the proposed concept. In this band the skin depth of gold is $0.72-0.59$ μm. The beams are designed to be at least 2 μm thick such that the Q_u is not severly degraded. Since the cavities are considered highly-loaded, the capacitive region between the post and the ceiling is primarily what dictates the operation frequency. The diameter of the post is chosen to be 300 μm in order to achieve Ku-band operation. The cavity depth is designed to be 4 mm in order to achieve the specified $Q_u > 800$ across the tuning frequency band. The capacitive gap between the ceiling and the post is chosen to be $5-6$ μm in order to have the initial resonant frequency be within the specified Ku-band. Closer gaps have been successfully demonstrated in the literature [18]. A $5-6$ μm capacitive gap represents a compromise between frequency tuning and repeatability. Finally, the cantilevers beams are designed with $w_b = 50$ μm, $L_b = 500$ μm and a post release tip deflection, h_0, of 50 μm in order to achieve > 50 % frequency tuning.

Figure 3 illustrates the full wave numerical simulation of the expected RF performance per the device parameters listed in table 1. Frequency tuning of over 50% is expected for an initial RF gap, g_{RF}, of 5 μm between the evanescent post and cantilever array and a tip deflection of 50 μm. Quality factors from $700-1400$ are possible. However, in order to achieve this high-Q_u, careful attention must be placed on the design of the DC bias-line to ensure RF energy does not leak through it [20]. Figure 4 is a simulation that illustrates the impact of the sheet resistance, R_B, of the SiCr bias-line on the unloaded quality factor (please see figure 1 for device structure).

2.3. Actuation

Electrostatic fringing-field forces are inherently weaker than electrostatic parallel-plate field forces. In order to facilitate reasonable applied bias voltages, low spring constant designs may be required. The EFFA cantilever beams are numerically modeled in CoventorWare [17] in order to investigate its electromechanical behavior.
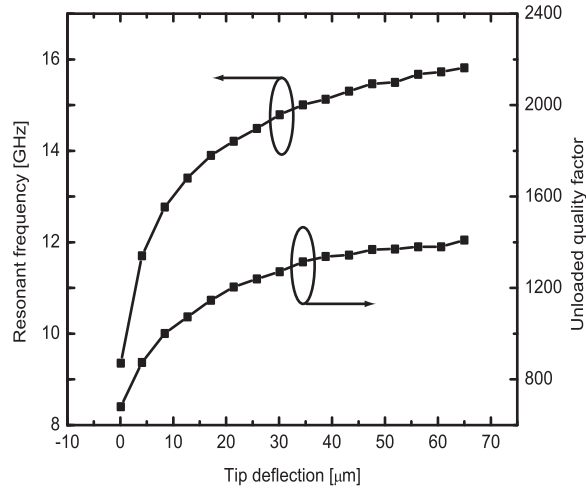
Figure 3. Simulated RF performance of final design per device parameters in table 1 (please refer to figure 1 for device structure).
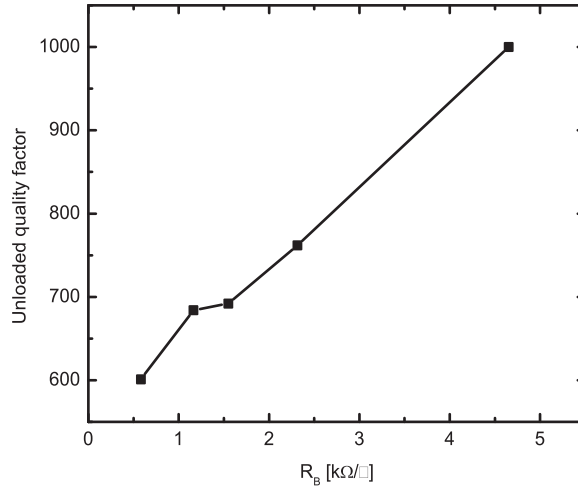

Figure 4. HFSS simulation of Q_u as a function of sheet resistance, R_B. $f_0 = 12.5$ GHz (please refer to figure 1 for device structure).

Figure 5 illustrates the simulated gap height versus applied bias voltage characteristics of the electrostatic fringing-field cantilevers. Figure 6 illustrates the simulated applied bias required to pull the cantilevers completely down versus lateral pull-down electrode spacing, s. Figure 7 illustrates the impact of the spring constant on V_{pd}, the voltage needed to pull the beams down completely flat with respect to the pull-down electrodes. As can be seen, the required bias voltage increases significantly when the beam thickness is increased beyond 1 μm which is indicative of the weaker electrostatic forces provided by fringing-field actuation when compared to traditional parallel-plate field actuation. A spring constant of 0.3 N/m is selected as a compromise between actuation voltage and Q_u ($t_b = 2$ μm $\rightarrow 2-3\times$ the Ku-band skin depth).
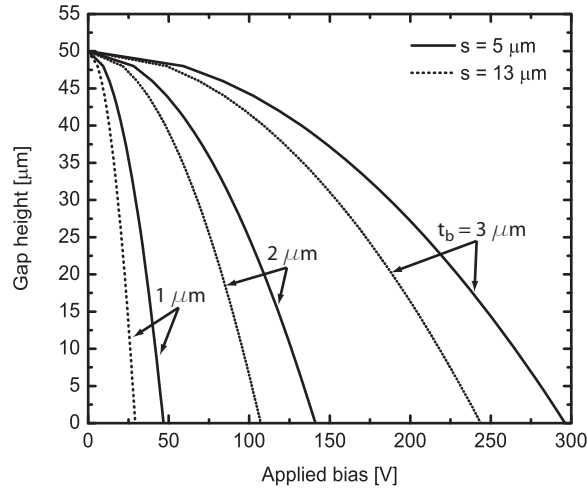
Figure 5. Simulated gap height versus applied bias voltage for cantilevers of various thicknesses, t_b. $w_b = 50$ μm and $L_b = 500$ μm.
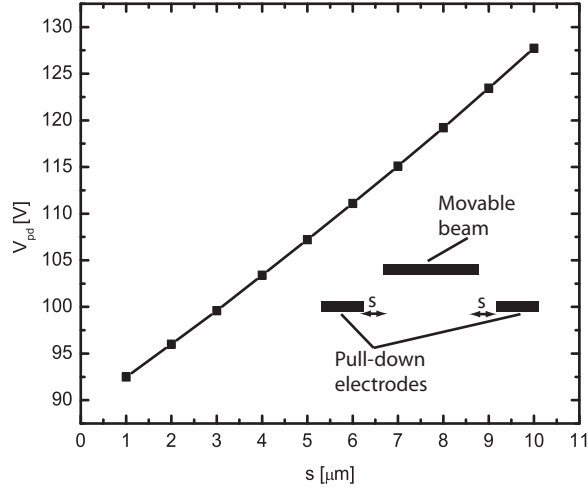

Figure 6. Simulated voltage needed for complete tip deflection as a function of horizontal gap s. $t_b = 2$ μm, $w_b = 50$ μm and $L_b = 500$ μm.

2.4. Switching Time

The noncontacting device design eliminates the pull-in instability of the resonator. However, the penalty paid for this design is a substantial decrease in mechanical damping coefficient, b, and an increase in the cantilever mechanical quality factor, Q_{cant}, which is indicative of a device with a long settling time (100s of microseconds to milliseconds). The damping of a rectangular or circular parallel-plate geometry can be expressed as [12]

$$b = \frac{3}{2\pi} \frac{\mu A^2}{g_0^3} \tag{1}$$

where A is the area of the MEMS membrane ($w_b \times L_b$), g_0 is the gap between the cantilever beam and the nearest damping surface. The symbol μ is the coefficient of viscosity and at standard atmospheric temperature and pressure is calculated to be
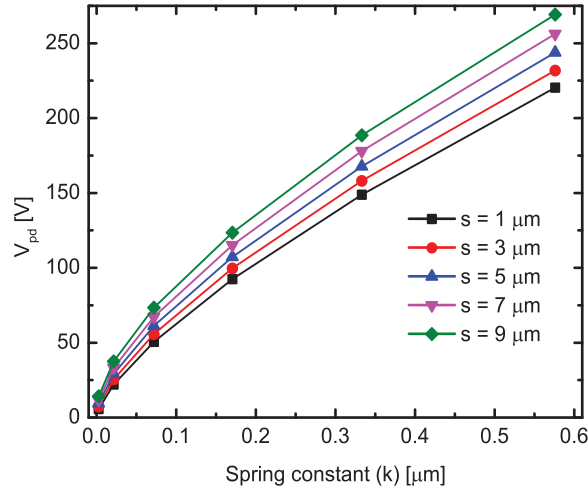
Figure 7. Calculated voltage needed for complete tip deflection as a function of spring constant k for various lateral gaps s.

1.845×10^{-5} kg/m·s based on the following expression [12]

$$\mu = 1.2566 \times 10^{-6}\sqrt{T}\left(1 + \frac{\beta_\mu}{T}\right)^{-1} kg/m \cdot s \qquad (2)$$

where $\beta_\mu = 110.33$ K and T is temperature in kelvin. The Q_{cant} can be approximated by the following expression [12]

$$Q_{cant} = \frac{\sqrt{E\rho}t_b^2}{\mu(w_b L_b)^2}g_0^3 \qquad (3)$$

where E is the Young's modulus of the beam material, ρ is the density of the beam material, and t_b is the beam thickness. It is readily observed that $b \propto g_0^{-3}$ and $Q_{cant} \propto g_0^3$. The presented MEMS tuners have the substrate completely removed from beneath the beams. As a result, g_0 is typically ≥ 20 μm. This correlates to a $b \simeq 0$ and a $Q_{cant} \geq 2$ due to the lack of squeeze film damping. Based on the low b and relatively high Q_{cant}, the cantilever beam is considered an inertia-limited system (acceleration limited). Therefore, we can use the following simplified closed-form expression to calculate the switching time for the cantilevers [12]

$$t_{down} \simeq 3.67\frac{V_{pd}}{2\pi V_{app}f_{m0}} \qquad (4)$$

where V_{app} is the applied bias which is typically $1.2-1.4V_{pd}$ to result in fast switching time. The mechanical resonant frequency of the beam is represented by f_{m0} and is calculated by the following expression

$$f_{m0} = \frac{1}{2\pi}\sqrt{\frac{k(1)}{m_{eff}}} \qquad (5)$$

We can calculate the effective mass, m_{eff}, of the cantilever beam from the following [21]

$$\frac{1}{2\pi}\sqrt{\frac{k(1)}{m_{eff}}} = \frac{\beta_f^2}{2\pi}\sqrt{\frac{EI}{\rho w_b t_b L_b^4}} \tag{6}$$

$$m_{eff}(1) = \frac{12\rho k(1)L_b^4}{\beta_f(1)^4 E t_b^2} \tag{7}$$

where $k(1)$ represents the first mode spring constant of the cantilever due to a distributed load applied over the entire beam

$$k(1) = \frac{2Ew_b}{3}\left(\frac{t_b}{L_b}\right)^3 \tag{8}$$

$\beta_f = [1.8751\ 4.6941\ 7.8548]$ represents the first three modes of a cantilever beam, and I is the moment of inertia for a cantilever beam ($I=w_b t_b^3/12$). The first mode effective mass, $m_{eff}(1)$ for a cantilever beam with $w_b = 50\ \mu$m, $L_b = 500\ \mu$m and $t_b = 2\ \mu$m is 6.2513 $\times\ 10^{-10}$ kg. The calculated f_{m0} is 2.6 kHz. Figure 8 shows the calculated switching time for the cantilever beams for multiple ratios of V_{app}/V_{pd}. Since the voltage needed to pull the cantilevers down are already in the $100-200$ V range, it will be difficult to go much higher in voltage to improve the speed. Therefore, we expect the switching time to be $\sim 180\ \mu$s for most of the analog states.

The release behavior can be approximated by (9) with a zero external force

$$m_{eff}(1)\frac{d^2x}{dt^2} + b\frac{dx}{dt} + k(1)x = 0 \tag{9}$$

Figure 9 illustrates the simulated dynamic response of the cantilever beam for various values of Q_{cant}. From the simulated response, it is observed that the cantilevers can be approximated as an under-damped second order system. For very low b, the physical mechanisms that provide damping is dissipation in the beam anchors and the interface granules in the beam itself [12]. Figure 9 clearly illustrates that the lack of squeeze film damping results in a settling time of several milliseconds. Employing DC-dynamic biasing waveforms that exploit the physics of the under-damped second order system can potentially improve the long settling time.

2.5. DC-Dynamic Biasing

The proposed DC-dynamic biasing waveform exploits the overshoot phenomena of under-damped second order systems in order to improve the settling time. Figure 10 illustrates the key metrics of an under-damped second order system in response to a unit-step input. The metrics are: final gap height, G_f, peak gap height, G_p, rise time, t_r, peak time, t_p, and settling time, t_s. Typically, t_r is defined as the time it takes to get from $0.01G_f$ to $0.9G_f$. While t_s is defined as the time it takes to get within 5 % of G_f. At G_p, the velocity of the beam is at a minimum. Therefore, applying a bias at the
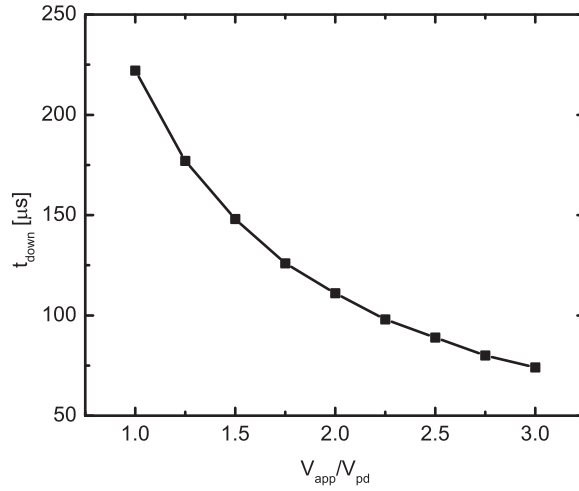
Figure 8. Calculated switching time of the EFFA cantilever tuners based on (4) geometrical parameters given in Table 1.
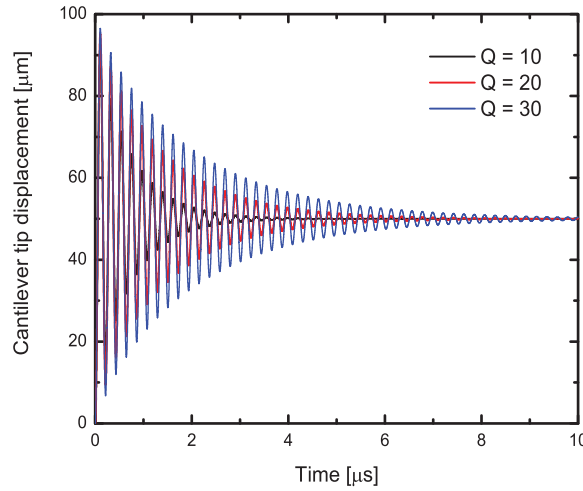

Figure 9. Simulated dynamic response of a cantilever with dimensions $w_b = 50$ μm, $L_b = 500$ μm and $t_b = 2$ μm for various Q_{cant} based on (9).

time the beam arrives at the peak gap will potentially improve the settling time of the beam.

Figure 11 illustrates a sketch of the DC-dynamic biasing waveform form concept. The red curve represents the DC-dynamic bias waveform while the black curve represents the deflection of the cantilever beam in response to the applied bias. The gap heights G_2 and G_4 are the peak gap heights of G_1 and G_3, respectively. These are determined by the desired electromagnetic resonant frequency. The times t_2 and t_4 are when the bias is applied to hold the beams at the G_2 and G_4 gap heights, respectively. The times t_1 and t_3 are user defined, however, $t_2 - t_1 = t_p$ and $t_4 - t_3 = t_p$. Lastly, the voltages V_1, V_2, V_3, and V_4 are the voltages needed to obtain the steady state gap heights G_1, G_2, G_3, and G_4, respectively. Both the voltages and gap heights are found through numerical simulation (please refer to Section 2.3)
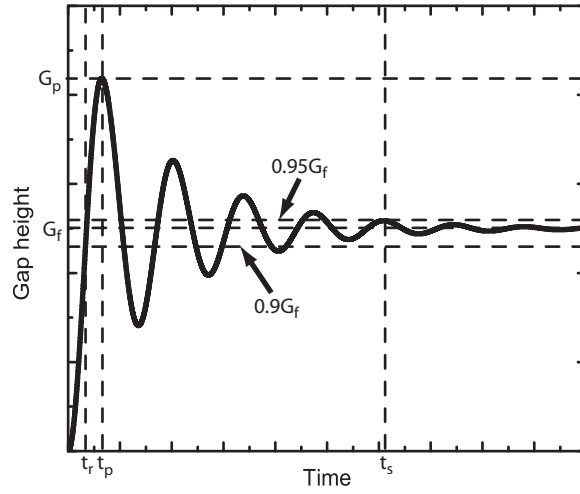
Figure 10. Sketch of typical under-damped second order system response to a unit-step input. Key metric are noted: peak gap G_p, final gap, G_f, rise time, t_r, peak time t_p, and settling time, t_s.
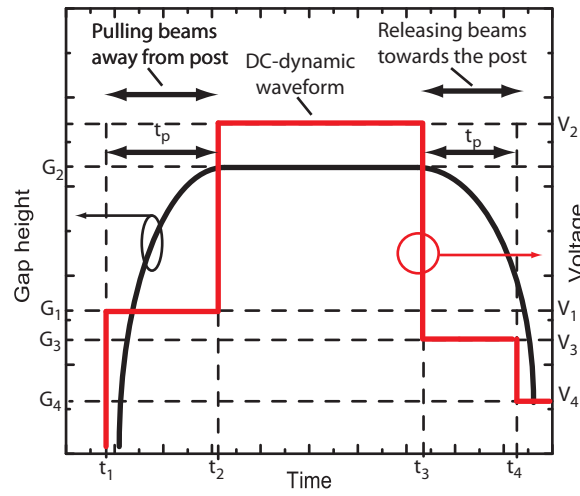

Figure 11. Sketch of typical cantilever beam response to an input DC-dynamic biasing waveform.

In order to find G_2 and G_4, the percent overshoot, $\%OS$, must be obtained. The overshoot in an under-damped second order system can be expressed in terms Q_{cant}. First, the damping ratio, ζ, is expressed as

$$\zeta = \frac{b}{2m_{eff}\omega_{m0}} \tag{10}$$

We can relate ζ to Q_{cant} by the following

$$\zeta = \frac{1}{2Q_{cant}} \tag{11}$$

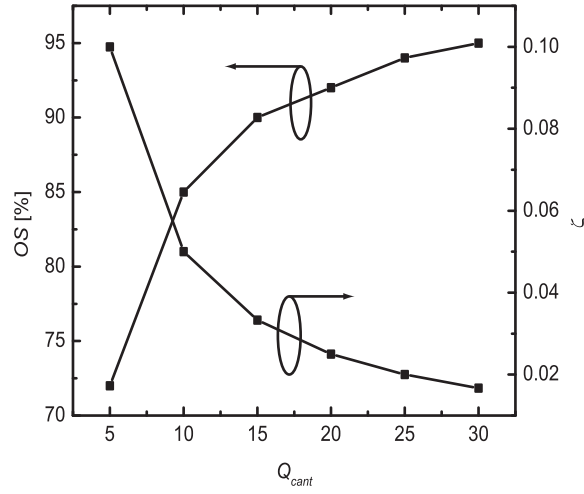The $\%OS$ can now be expressed in terms of Q_{cant}

Figure 12. Calculated percent overshoot, %OS, and damping ratios, ζ, for various mechanical damping factors, Q_{cant} based on (11) and (12).

$$\%OS = 100 \times e^{\frac{-\zeta\pi}{\sqrt{1-\zeta^2}}} = 100 \times e^{\frac{-\frac{\pi}{2Q_{cant}}}{\sqrt{1-(\frac{1}{2Q_{cant}})^2}}} \tag{12}$$

We can express t_r as

$$t_r = \frac{2.16(\frac{1}{2Q_{cant}}) + 0.6}{\omega_{m0}} \tag{13}$$

The t_p can be expressed as the following

$$t_p = \frac{\pi}{\omega_{m0}\sqrt{1-\zeta^2}} = \frac{\pi}{\omega_{m0}\sqrt{1-(\frac{1}{2Q_{cant}})^2}} \tag{14}$$

Lastly, we can calculate t_s (5 % of steady state value) as a function of Q_{cant}

$$t_s \approx \frac{3}{\zeta\omega_{m0}} \approx \frac{6Q_{cant}}{\omega_{m0}} \tag{15}$$

We can obtain an approximate value for Q_{cant} based on t_s from simulation or measurements. Figure 12 illustrates how ζ and %OS change as a function of Q_{cant}. Figure 13 illustrates the impact of Q_{cant} on the settling time. For a cantilever with a $Q_{cant} = 20$ and $f_{m0} = 2.6$ kHz, $t_p = 190$ μs, $t_r = 39.5$ μs, and %$OS = 92.4$. Tables 2 and 3 shows the calculated voltage and timing parameters, respectively, for an example DC-dynamic waveform based on figure 11.

3. Fabrication

Figure 14 summarizes the four-mask process that is necessary for the fabrication of electrostatic fringing-field cantilever tuners. The cantilevers are fabricated on a high-resistivity silicon substrate ($\sim$10 kΩ-cm) with a thickness of 525 μm and 5000 Å of
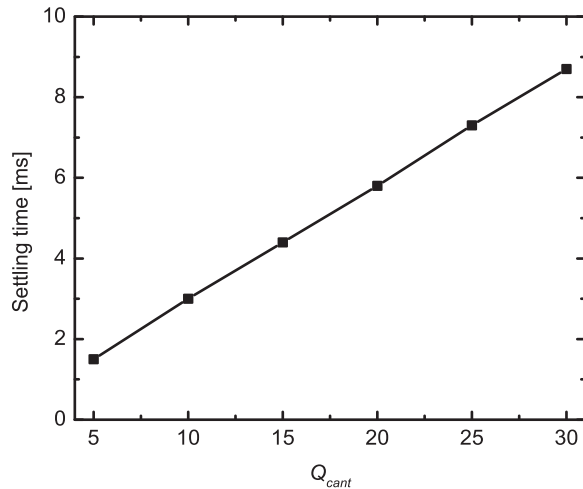
Figure 13. Calculated settling time for proposed cantilever tuners based on (15).

Table 2. Designed Voltage Parameters of DC-Dynamic Bias Waveform

State	V_1	V_2	V_3	V_4
60 V	44 V	60 V	44 V	12 V
80 V	58 V	80 V	58 V	17 V
100 V	73 V	100 V	73 V	21 V
120 V	87 V	120 V	87 V	21 V
140 V	100 V	140 V	100 V	27 V
160 V	115 V	160 V	115 V	30 V

Table 3. Designed Time Parameters of DC-Dynamic Bias Waveform

t_1	t_2	t_3	t_4
0 μs	187 μs	18 ms	18.187 ms

thermally grown SiO_2. The fabrication begins with patterning the SiO_2 with buffered hydrofluoric acid. This etch is used to expose the silicon which serves as the sacrificial layer for the final release of the fringing-field cantilevers. Next, 1000 $\mathring{A}$ SiCr is deposited to serve as a high resistivity DC bias-line ($\sim$2150 S/m) in order to mitigate RF leakage. Gold is sputter deposited to 2 μm thick which serves as the primary metal for the cantilever beams and the rest of the cavity ceiling. A very thin ($<$20 nm) titanium adhesion layer is also included. A SU-8 layer is spun at 3000 rpm to a thickness of 5.75 μm and serves as a dielectric layer to prevent shorting with the cavity metal. A dry isotropic XeF_2 etch that selectively attacks the silicon and releases the gold cantilevers is the final step. Figure 15 shows the SEM of the final released cantilever beam array.

Compared to current RF-MEMS designs for reconfigurable components the proposed fringing-field tuners have a relatively simple fabrication process, inherently-robust device design and the potential for extremely-high fabrication yield. After device fabrication, the cantilever tuners are placed on top of the machined resonant copper
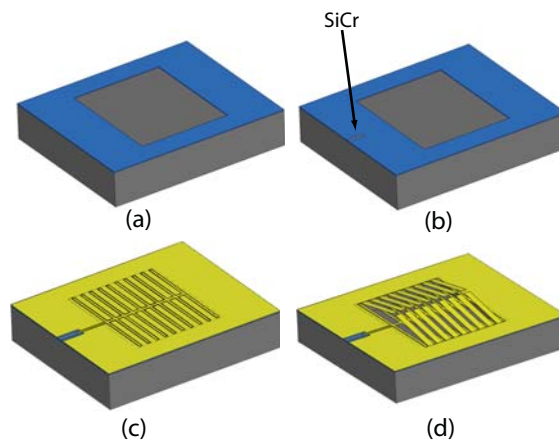
Figure 14. Fabrication sequence of electrostatic fringing-field actuators. (a) Pattern silicon dioxide, (b) deposit SiCr for DC bias-line, (c) flood deposit and pattern gold for cantilevers and pull-down electrodes and (d) XeF$_2$ dry etch release of cantilever beams.
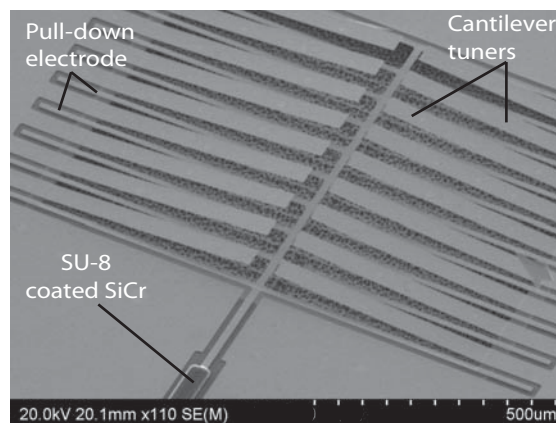

Figure 15. Scanning electron micrograph of electrostatic fringing field cantilever array.

cavity. For the detailed assembly procedure of the MEMS tuner array with the copper cavity please refer to [6].

4. Measurements and Discussion

4.1. RF Measurement

The resonator measurements are performed with an Agilent E8361A network analyzer. The input power of the signal used in this study is -17 dBm. A static resonator, with released cantilever beams and without the SiCr DC bias-line, is first designed, fabricated, and measured in order to quantify the impact of the spatial distribution of the cantilevers on the Q_u. The resonator is designed to be weakly coupled for accurate Q_u extraction. Figure 16 is a comparison between the simulated and measured resonators. The numerical simulations are for both a resonator that has beams and
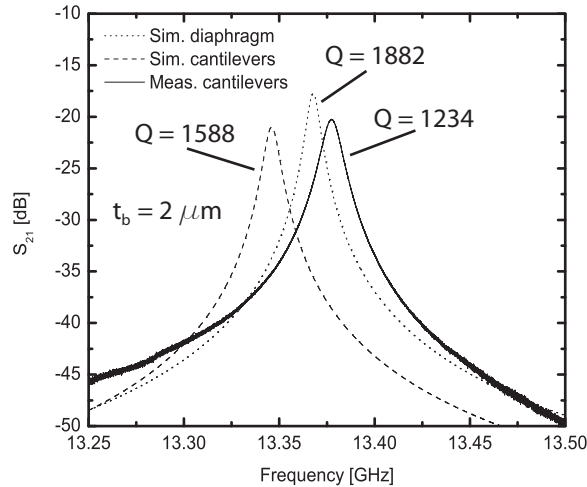
Figure 16. Comparison of measured resonator without SiCr DC bias-line to numerical simulation of the resonator with and without cantilever beams. The simulated metal thickness is $t_b = 2$ μm (Please refer to figure. 1 for the device structure).

a solid diaphragm. The measured Q_u of the resonator is 1234 at 13.4 GHz. When compared to the numerical simulation, a 20.7 % and 34.4 % reduction in Q_u is observed for cavities with and without beams, respectively.

A tunable resonator based on the parameters in table 1 is designed, fabricated, and measured. The measured tunable RF performance is illustrated in figure 17. Like the static resonator, the tunable resonator is designed to be weakly coupled for accurate Q_u extraction. Due to fabrication tolerance issues in machining copper for the resonator cavity, the post top was not flat and limited the tuning range to 20 % from $12.5-15.5$ GHz. Figure 18 illustrates this point. In addition, a fabrication issue due to contamination of the DC sputtering system utilized to deposit the bias-line prevented the manufacturing of a high sheet resistance DC bias-line of > 800 $\Omega/\square$. The resulting line was only 200 $\Omega/\square$ (bias-line resistance of 23.4 kΩ). The measured Q_u was limited to $280-515$ from $12.5-15.5$ GHz.

4.2. Switching Time Measurement

Figure 19 illustrates the core measurement setup for applying the DC-dynamic bias waveform and measuring the settling time of EFFA cantilever tuned resonators. The function generator is connected to a linear high voltage high speed amplifier in order to achieve the necessary voltages to actuate the electrostatic fringing-field cantilevers. The settling time of the analog tunable resonator is measured in real time with a network analyzer with a CW time sweep.

Figure 20 illustrates the switching time of the tunable resonator for a standard unit step and DC-dynamic input. By using the DC-dynamic bias waveform, the settling time reduces from ~ 8 ms down to 190 μs and 148 μs for up-to-down and release states, respectively. Since the cantilever beams are inertia-limited, due to the damping
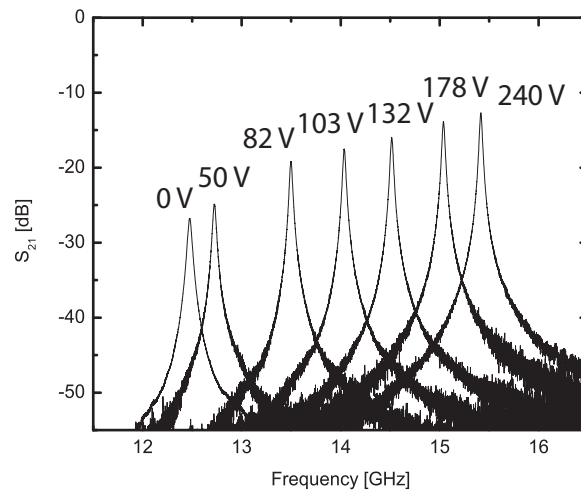
Figure 17. Measured frequency response of electrostatic fringing-field tunable resonator at various applied biases.
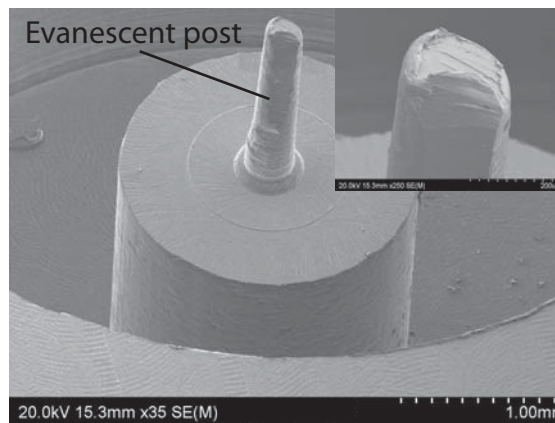

Figure 18. Scanning electron micrograph of machined copper evanescent post.
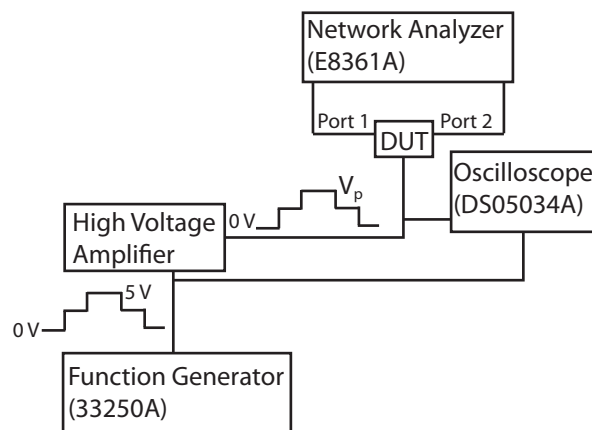

Figure 19. Measurement setup for switching time.

conditions, improvements in the switching time can be made by simply reducing the mass of the cantilever beams. For example, this can be performed by reducing the width of
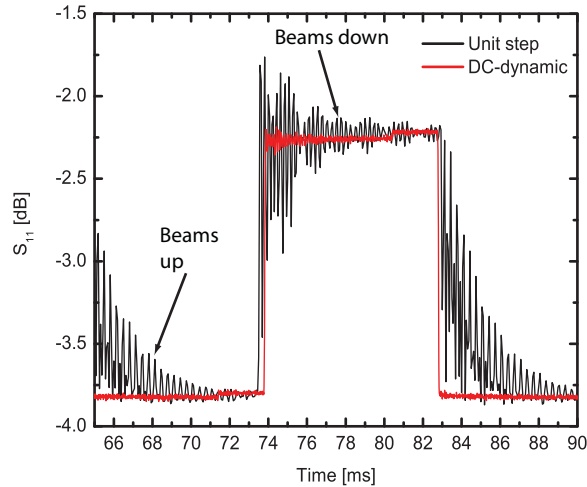
Figure 20. Resonator total settling time in response to a typical unit step and DC-dynamic applied bias.

the cantilever. However, care must be taken when making this modification due to the inherent interdependence between the unloaded electromagnetic quality factor and the series resistance introduced by the cantilever beam geometry.

The switching times are illustrated in figures 21 and 22. Figure 23 illustrates how the DC-dynamic bias waveform can be used for all analog positions of the tunable resonator. Tables 4 and 5 show the voltages and times, respectively, used to achieve all the states shown in figure 23. The applied biases and timing were found in real-time by viewing the network analyzer and making manual adjustments on the arbitrary waveform generator as the beams were actuating. Additional bias steps on the release phase were required in order to reduce the ringing.

The discrepancies between the calculated and measured result are due to the time step resolution of the function generator used to create the DC-dynamic bias waveform. Based on the calculations, a time step resolution of < 1 μs is needed. The function generator used in this study only provided a 10 μs resolution. As a result, the voltage steps were not applied at the precise calculated timings that are defined by the geometry and damping conditions of the cantilever beam. Using a function generator with a finer time step resolution will most likely decrease the discrepancy between the actual and designed voltage and time parameters. Nevertheless, it is observed that the calculated and measured values are in good agreement.

5. Conclusion

This paper presents the design, fabrication and measurement of an pull-in free tunable microwave resonator based on electrostatic fringing-field actuated cantilever tuners. The fringing-field topology is inherently-robust due to its total lack of contacting surfaces and dielectric layers. A continuously tunable resonator from $12.5-15.5$ GHz with an unloaded quality factor of $280-515$ is demonstrated. DC-dynamic biasing is utilized
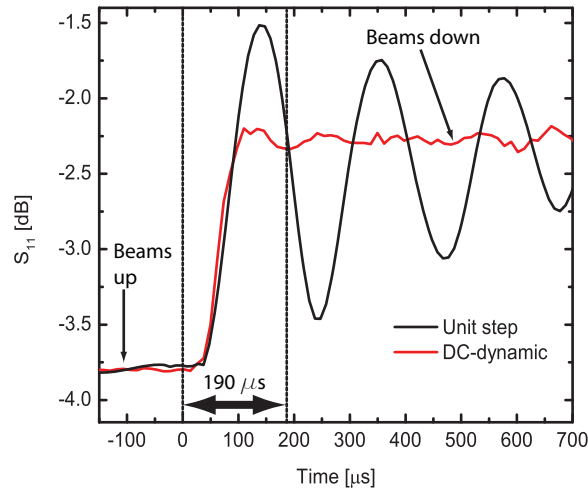
Figure 21. Measured up-to-down switching time of the tunable resonator in response to both a typical unit step and DC-dynamic applied bias.
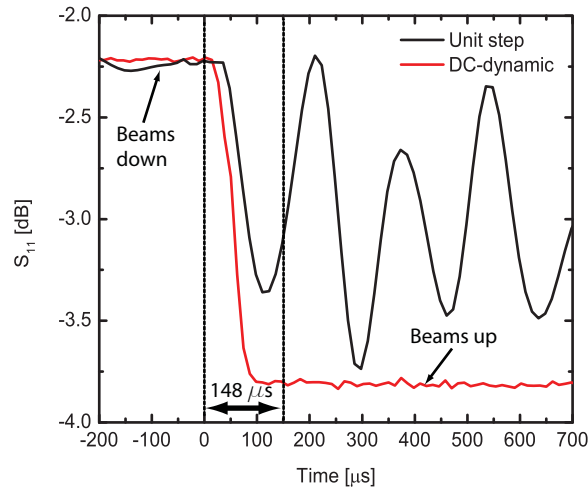

Figure 22. Measured down-to-up switching time of the tunable resonator in response to both a typical unit step and DC-dynamic applied bias.

Table 4. Voltage Parameters of DC-Dynamic Bias Waveform

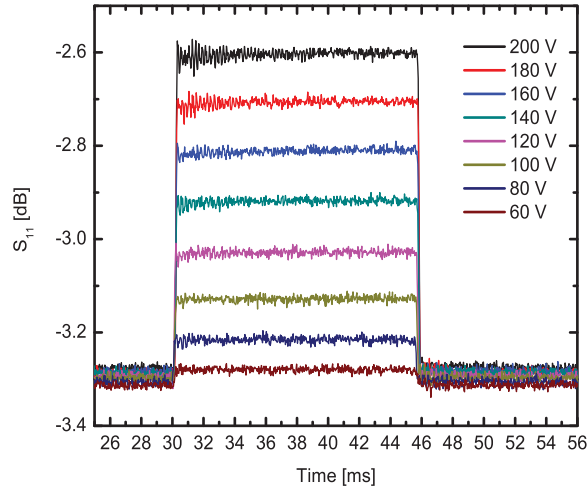| State	V_1	V_2	V_3	V_4	V_5	V_6
60 V	0 V	52 V	60 V	52 V	50 V	40 V
80 V	0 V	60 V	80 V	80 V	60 V	40 V
100 V	0 V	72 V	100 V	72 V	60 V	40 V
120 V	0 V	86 V	120 V	86 V	60 V	40 V
140 V	0 V	92 V	140 V	92 V	60 V	40 V
160 V	0 V	102 V	160 V	102 V	60 V	40 V
180 V	0 V	112 V	180 V	114 V	60 V	40 V
200 V	0 V	118 V	200 V	114 V	60 V	40 V

Figure 23. Measured switching time of tunable resonator for various analog states in response to the DC-dynamic applied bias.

Table 5. Time Parameters of DC-Dynamic Bias Waveform

State	t_1	t_2	t_3	t_4	t_5
60	10 μs	190 μs	18.01 ms	18.19 ms	18.21 ms
80	20 μs	190 μs	18.02 ms	18.19 ms	18.21 ms
100	20 μs	190 μs	18.02 ms	18.19 ms	18.21 ms
120	30 μs	190 μs	18.05 ms	18.19 ms	18.21 ms
140	30 μs	190 μs	18.05 ms	18.19 ms	18.21 ms
160	40 μs	190 μs	18.05 ms	18.19 ms	18.21 ms
200	50 μs	190 μs	18.05 ms	18.19 ms	18.21 ms

to improve the switching time of the resonator by one order of magnitude. The up-to-down and down-to-up time is 190 μs and 148 μs, respectively. Future work includes investigating power handling and linearity of the presented EFFA tunable resonator.

Acknowledgments

References

[1] Joshi H, Sigmarsson H H, Peroulis D and Chappell W J, 2007 *IEEE MTT-S Int. Microw. Symp. Tech. Dig.* 2133−36

[2] Rebeiz G, Entesari K, Reines I C, Park S, El-Tanani M A, Grichener A and Brown A R, 2009 *IEEE Microwave Mag.*, **10** 55−72

[3] Park S-J, Reines I, Patel C and Rebeiz G M, 2010 *IEEE Trans. Microw. Theory Tech.*, **58** 381−89

[4] Liu X, Katehi L P B, Chappell W J and Peroulis D, 2010 *J. Microelectromech. Syst*, **19** 774−84

[5] Liu X, Katehi L P B, Chappell W J and Peroulis D, 2009 *IEEE MTT-S Int. Microw. Symp. Tech. Dig.*, 1149−1152

[6] Irshad W and Peroulis D, 2011 *IEEE MTT-S Int. Microwave Symp. Dig.*, doi: 10.1109/MWSYM.2011.5972971

[7] Arif M S, Irshad W, Liu X, Chappell W J and Peroulis D, 2011 *IEEE MTT-S Int. Microwave Symp. Dig.*, doi: 10.1109/MWSYM.2011.5972966

[8] Arif M S and Peroulis D, 2012 *IEEE MTT-S Int. Microwave Symp. Dig.*, Accepted

[9] Small J, Irshad W, Chappell W J and Peroulis D, 2012 *IEEE MTT-S Int. Microwave Symp. Dig.*, Accepted

[10] Liu X, Small J, Berdy D, Katehi L P B, Chappell W J and Peroulis D, 2011 *IEEE Microw. Wireless Compon. Lett.*, **21** 406−08

[11] Stefanini R, Martinez J D, Chatras M, Pothier A, Boria V E and Blondy P, 2011 *IEEE Microw. Wireless Compon. Lett.*, **21** 237−39

[12] Rebeiz G M, 2003 *RF MEMS: Theory, Design and Technology* (New York: Wiley)

[13] Gong S, Reck T and Barker N S, 2010 *40th European Microwave Conference* 1114-17

[14] Patel C D and Rebeiz G M, 2011 *IEEE MTT-S Int. Microwave Symp. Dig.* doi:10.1109/MWSYM.2011.5972717

[15] Rosa M A, Bruyker D D, Völkel A R, Peeters E and Dunec J, 2004 *J. Micromech. Microeng.*, **14** 446−51

[16] Garg A, Small J, Mahapatro A, Liu X, Peroulis D, 2009 *IEEE Sensors* 1052−55.

[17] CoventorWare, http://www.coventor.com

[18] Moon S, Sigmarsson H, Joshi H and Chappell W J, 2010 *IEEE Microw. Wireless Compon. Lett.* **20** 450−52

[19] Ansoft, http://www.ansoft.com/

[20] Park S-J, El-Tanani M A, Reines I and Rebeiz G M, 2008 *IEEE Trans. Microw. Theory Tech.* **56** 2248-2355

[21] Meirovitch L, 1997 *Principles and Techniques of Vibration, 2nd ed.*, (Englewood Cliffs, NJ: Prentice Hall)